How Well Do Climate Models Reproduce North Atlantic Subtropical Mode Water?

SHENFU DONG

Cooperative Institute for Marine and Atmospheric Studies, University of Miami, and NOAA/Atlantic Oceanographic and Meteorological Laboratory, Miami, Florida

KATHRYN A. KELLY

Applied Physics Laboratory, University of Washington, Seattle, Washington

(Manuscript received 7 November 2012, in final form 8 April 2013)

ABSTRACT

Formation and the subsequent evolution of the subtropical mode water (STMW) involve various dynamic and thermodynamic processes. Proper representation of mode water variability and contributions from various processes in climate models is important in order to predict future climate change under changing forcings. The North Atlantic STMW, often referred to as Eighteen Degree Water (EDW), in three coupled models, both with data assimilation [GFDL coupled data assimilation (GFDL CDA)] and without data assimilation [GFDL Climate Model, version 2.1 (GFDL CM2.1), and NCAR Community Climate System Model, version 3 (CCSM3)], is analyzed to evaluate how well EDW processes are simulated in those models and to examine whether data assimilation alters the model response to forcing. In comparison with estimates from observations, the data-assimilating model gives a better representation of the formation rate, the spatial distribution of EDW, and its thickness, with the largest EDW variability along the Gulf Stream (GS) path. The EDW formation rate in GFDL CM2.1 is very weak because of weak heat loss from the ocean in the model. Unlike the observed dominant southward movement of the EDW, the EDW in GFDL CM2.1 and CCSM3 moves eastward after formation in the excessively wide GS in the models. However, the GFDL CDA does not capture the observed thermal response of the overlying atmosphere to the ocean. Observations show a robust anticorrelation between the upper-ocean heat content and air–sea heat flux, with upper-ocean heat content leading air–sea heat flux by a few months. This anticorrelation is well captured by GFDL CM2.1 and CCSM3 but not by GFDL CDA. Only GFDL CM2.1 captures the observed anticorrelation between the upper-ocean heat content and EDW volume. This suggests that, although data assimilation corrects the readily observed variables, it degrades the model thermodynamic response to forcing.

1. Introduction

The oceans play a central role in regulating the weather and global climate system through their storage and transport of heat, in particular in the regions where the oceans are strongly coupled to the atmosphere. In the North Atlantic the intense air–sea interaction occurs in the Gulf Stream (GS) region, the northwestern portion of the subtropical gyre. The potential important influence of the Gulf Stream system on climate is mostly provided by the large wintertime heat release from the ocean to the atmosphere, which is supplied by the heat advected from the tropics through the GS and by the heat stored in the ocean. One of the most important processes involving the intense air–sea interaction is the formation of the subtropical mode water (STMW), often referred to as Eighteen Degree Water (EDW) in the western North Atlantic because of its nearly constant temperature. The STMW is of particular importance in climate processes because it temporally integrates the ocean's response to air–sea fluxes, stores heat from one year to the next, and forces turbulent heat fluxes, providing a rare example of ocean feedback in the midlatitudes (de Coëtlogon and Frankignoul 2003; Kelly et al. 2010).

The EDW is the dominant feature of the upper-ocean thermal structure in the western North Atlantic with a typical thickness of 250 m (Worthington 1995; McCartney 1982). The EDW is formed by deep convection just south of the Gulf Stream in a region with strong wintertime

Corresponding author address: Shenfu Dong, CIMAS/University of Miami/NOAA, 4301 Rickenbacker Causeway, Miami, FL 33149. E-mail: shenfu.dong@noaa.gov

DOI: 10.1175/JPO-D-12-0215.1

cooling. After its formation, EDW is subsequently subducted below the surface mixed layer and is seasonally isolated from interaction with the atmosphere. EDW formed in one winter can interact with the atmosphere in subsequent winters through entrainment into the mixed layer. With their large heat content and their ability to retain a year-to-year memory of property variations as a result of changing forcing conditions (Alexander and Deser 1995; Timlin et al. 2002), mode waters represent an integrator of seasonal climate variations (Talley and Raymer 1982; Talley and McCartney 1982; Hanawa and Talley 2001). Therefore, changes in EDW properties reflect variations in climatic conditions.

The EDW is not simply an integrator of the changing forcing; it can impose a thermal forcing back on the overlying atmosphere through the surface heat exchange. Previous studies (Kwon 2003; Dong et al. 2007; Douglass et al. 2013) suggested that the EDW volume is anticorrelated with the upper-ocean heat content, meaning that more EDW implies lower upper-ocean heat content. Thus, the EDW volume is an indicator of the amount of heat stored in the upper ocean. Dong and Kelly (2004) found a correlation between the upper-ocean (upper 800 m) heat content and heat loss to the atmosphere in the GS region, suggesting that variations in the ocean heat storage and EDW can force air–sea heat fluxes. Furthermore, Joyce et al. (2000) suggested that north–south shifts of the GS position are associated with changes in the EDW. The north–south shifts of the GS could influence the midlatitude storms (Nakamura and Yamane 2009). Thus, a better understanding of the processes involved in EDW changes is important for climate systems.

Changes in EDW volume involve a number of dynamic and thermodynamic processes, including formation, dissipation, and subduction/advection. A large field program over a 2-yr period (2004–06), the Climate Variability and Predictability (CLIVAR) Mode Water Dynamic Experiment (CLIMODE) as well as related modeling efforts (Marshall et al. 2009), is dedicated to advancing our understanding of the EDW formation and its subsequent evolution. The goal of the CLIMODE field program is to observe and quantify the various processes that contribute to EDW variations. Analyses of CLIMODE observations have revealed new perspectives regarding EDW formation. Joyce et al. (2013) suggested that convective processes are responsible for much of the formation within the GS. Using the moored data in the Sargasso Sea, Davis et al. (2013) found that restratification by lateral eddy heat fluxes from the GS can contribute to EDW anomalies by decreasing outcrop area, which in turn decreases the EDW formation rate. Based on observations and observational synthesis for the period 2004–06, Forget et al. (2011) examined the seasonal evolution of the EDW and suggested that approximately $\frac{2}{3}$ of the newly formed EDW was removed by restratification through air–sea heat fluxes and $\frac{1}{3}$ was dissipated by mixing. Maze and Marshall (2011) showed that heat flux effects (in a wide outcropping region) dominate over the frontal/Ekman effects (within the GS) in EDW formation; estimates of EDW formation from climatology by Olsina et al. (2013) and from an eddy-resolving numerical simulation by Maze et al. (2013) are also consistent with this conclusion. Kelly and Dong (2013) characterized the processes contributing strongly to interannual-to-decadal variations of EDW and thereby to provide guidance for evaluating climate models. They demonstrated that the EDW volume anomalies can be explained by formation over the 17°–19°C outcrop and by loss by mixing in the formation region, parameterized by the meandering of the GS.

Coupled atmosphere–ocean models are used to study climate variability on seasonal-to-centennial time scales and the predictability of the climate system. Numerous studies have used climate models to examine the dynamical effect of mode waters on ocean circulation and their response to climate changes (e.g., Xie et al. 2011; Xu et al. 2012a,b). However, despite the improvement of those climate models in recent years, studies (e.g., Suga et al. 2004; Thompson and Cheng 2008) have found large biases in water mass properties in those climate models. The ability of coupled climate models to capture the interactions among climate systems and to predict future climate change depends on both the representation of oceanic processes and the ability of the model atmosphere to respond to persistent ocean temperature anomalies. Thus, it is essential to assess the ability of climate models in reproducing oceanic processes. As an integrator of climate variations and a heat reservoir in the coupled climate system, the ability to reproduce mode water anomalies is a good target for numerical models. A better representation of mode water not only helps to improve the numerical models, but also benefits studies to advance our understanding of mode water processes.

Many efforts and resources have been focused on assimilation of observations. While data assimilation may correct the variables that are readily observed, it may change the relationship between forcing and response. In this study, we examine the distribution and variability of the EDW in three coupled climate models to evaluate their representation of oceanic physics and atmosphere–ocean coupling. Models both with and without data assimilation are used to examine to what extent the data-assimilation process alters the coupling between atmosphere and ocean.

In section 2 we describe the observations used to calculate formation and EDW volume, and the models evaluated in this study. The time mean and variability of the EDW and formation as well as their spatial distribution are examined in section 3. Results from the models are compared with estimates from observations in this section to evaluate the performance of the models. Discussion and conclusions are presented in sections 4 and 5, respectively.

2. Data and models

This study is focused on the domain in the western North Atlantic (20°–50°N, 80°–30°W). Observations used in this study include sea surface temperature (SST), upper-ocean temperature data, sea surface height (SSH), and turbulent and radiative heat fluxes. The SST and turbulent fluxes from objectively analyzed air–sea fluxes (OAFlux; Yu and Weller 2007) and the radiative fluxes from the International Satellite Cloud Climatology Project (ISCCP; Schiffer and Rossow 1983) that show better comparison with observations from a mooring from CLIMODE (Bigorre et al. 2013) are used to examine the transformation and formation of EDW. The combined monthly maps of net surface heat flux Q_{net} for 1985–2007 are on a 1° × 1° latitude–longitude grid.

The temperature data used in EDW volume estimates are from the National Oceanographic Data Center (NODC). They are derived from historical hydrographic data, the World Ocean Database (WOD), using objective mapping (Levitus et al. 2009). The gridded temperature data are available on a 1° grid with 3-month temporal resolution with seasons defined using the oceanographic convention [January–March (JFM), April–June (AMJ), July–September (JAS), and October–December (OND)]. There are a total of 16 vertical levels from the sea surface to a depth of 700 m, with the interval between layers increasing from 10 m at the sea surface to 100 m at depth. In addition, the monthly temperature data from Argo (Roemmich and Owens 2000) are used to better resolve the seasonal variation of the EDW. The gridded Argo temperature data from Scripps Institution of Oceanography (Roemmich and Gilson 2009) are available on a 1° grid for the period 2004–11. The 8-yr monthly gridded Argo fields are downloadable (http://www.argo.ucsd.edu/Gridded_fields.html). The volume of EDW is estimated from temperature profiles at each grid point following two criteria (Kwon and Riser 2004): the temperature must be within the range of 17°–19°C and the temperature gradient must be no greater than 0.006°C m^{-1}.

Following recent studies (Maze et al. 2009; Forget et al. 2011; Kelly and Dong 2013), the formation of EDW is determined based on the Walin framework (Walin 1982). Detailed information for the definition and calculation of EDW formation can be found in Kelly and Dong (2013). Here, we briefly describe the method used in this study to compute the EDW formation rate. The EDW formation rate ΔF is computed as the difference of volume fluxes into $F(19°)$ and out of $F(17°)$ the temperature class of 17°–19°C. The volume flux through an isotherm T_i at each time t, namely the transformation rate $F(T_i, t)$, is defined as the integration of net surface heat fluxes Q^i_{net} within the outcrops of temperature class T_i:

$$F(T_i, t) = \frac{-1}{\rho c_p \Delta T} \sum_i Q^i_{\text{net}}(t) A_i(t),$$

where the outcrop A_i corresponds to the temperature interval between $T_i + \Delta T/2$ and $T_i - \Delta T/2$. Following Maze et al. (2009) and Kelly and Dong (2013), the temperature interval ΔT is chosen as 0.5°C.

The GS path was derived from the locations of velocity maxima at each longitude. The geostrophic velocity fields are derived from altimetric SSH, which is produced by Archiving, Validation, and Interpretation of Satellite Oceanographic data (AVISO); the data are available weekly on a 1/3° × 1/3° grid (Ducet et al. 2000). The total SSH was derived by combining the anomalous SSH from altimeter and the time-mean SSH derived from a combination of Gravity Recovery and Climate Experiment (GRACE) and in situ data (Rio and Hernandez 2004).

Outputs from three different coupled climate models are analyzed: the Geophysical Fluid Dynamics Laboratory (GFDL) coupled data assimilation (GFDL CDA); Intergovernmental Panel on Climate Change (IPCC) Fourth Assessment Report (AR4) twentieth-century run of the GFDL Climate Model, version 2.1 (hereafter GFDL CM2.1); and the IPCC AR4 twentieth-century run of the National Center for Atmospheric Research (NCAR) Community Climate System Model, version 3 (CCSM3). The GFDL CDA applied a two-step data-assimilation procedure using an ensemble Kalman filter under a local least squares framework to GFDL CM2.1. The GFDL CDA was run from 1979 to 2007, with air temperature and winds from National Centers for Environmental Prediction (NCEP)–NCAR reanalysis assimilated in its atmospheric component, and SST, hydrographic data, and Argo float profiles assimilated in its oceanic component (Zhang et al. 2009). The oceanic component of GFDL CDA and GFDL CM2.1 is the fourth version of the Modular Ocean Model, version 4 (MOM4), configured with 50 vertical layers and 1° by 1° horizontal resolution with the meridional resolution

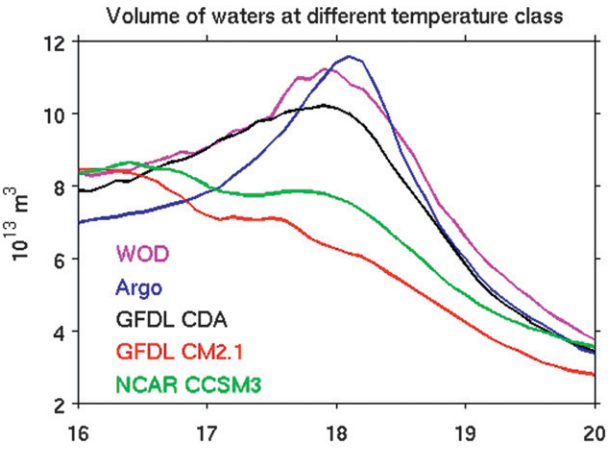

FIG. 1. Volume of waters at different temperature classes (°C) from observations (WOD: magenta, Argo: blue) and models (GFDL CDA: black; GFDL CM2.1: red; and CCSM3: green).

equatorward of 30° telescoping from 1° to 1/3° near the equator. The ocean component of CCSM3 is based on the Parallel Ocean Program (POP), version 1.4.3, which has 40 vertical layers and a 0.5° latitude by 1° longitude grid with the meridional resolution equatorward of 30° telescoping from 0.5° to 0.3° near the equator. Only the last 50 years of the GFDL CM2.1 and CCSM3 outputs are analyzed to compare with data-assimilation GFDL CDA and with observations. No significant differences in the results were found when the entire time series (1861–2000) was used. Publicly available monthly model outputs are analyzed in this study. For further details on the models, readers are referred to Zhang et al. (2007) for GFDL CDA, Delworth et al. (2006) for GFDL CM2.1, and Danabasoglu et al. (2006) for CCSM3.

3. Results

Before we assess the performance of the models in simulating the EDW and formation processes, the proper temperature class for EDW in models is examined. The EDW has been traditionally determined from waters within 17°–19°C isotherms. However, models may have temperature biases resulting in different temperature ranges for the EDW. To determine the appropriate temperature corresponding to the EDW in each model, we use the original definition of mode water, which is the temperature corresponding to the mode of a histogram by temperature class. The histograms of volume by temperature class for the region 20°–50°N and 80°–20°W (Fig. 1) show peaks around 18°C for both Argo and WOD data and also for GFDL CDA, which is not surprising because it assimilates observations. The volumes of water for GFDL CM2.1 and CCSM3 increase with decreasing temperature with peak volumes for temperatures below 16.5°C. However, both models show local peaks in the histogram at around 18°C. The local peak from GFDL CM2.1 is at a slightly lower temperature, but it is well within the 17°–19°C range. Using a lower temperature range (16.5°–18.5°C) to define the mode water in the models would result in an eastward shift of the region with thick EDW, away from the western North Atlantic where the EDW is generally formed. Examples of vertical temperature sections along 55°W clearly show that the thermostad is well within the temperature range 17°–19°C (Fig. 2) for both observations and models. Additional support for the use of a single temperature range for EDW comes from an examination of transformation rates (not shown) showing peak values around 19°C, consistent with results from observations. Thus, the same temperature range (17°–19°C) is used to estimate the EDW from observations and from models in this study.

Results from analyses of observations and model outputs are compared in the following subsections. First, we focus on the time-mean EDW volume/thickness and formation rate. Then seasonal variations in these variables are shown, followed by a comparison of variability to assess how well EDW volumes and formation rates are simulated in the models. We note that the analyses of temporal variability are based on the variables after removing their seasonal cycles. The significance of the correlation analysis is relative to the 95% significance level, given in parenthesis.

a. Time mean

The time series of the EDW volume from WOD and all three models are given in Fig. 3. The time-mean values of EDW volume and formation from observations and models are listed in Table 1. The mean volume of the EDW estimated from WOD is about $4.71 \times 10^{14}\,m^3$ with a standard deviation of $1.12 \times 10^{14}\,m^3$. The data-assimilation GFDL CDA gives a slightly larger mean EDW volume but comparable standard deviation of $5.25\ (\pm\ 1.09) \times 10^{14}\,m^3$. The EDW volumes from GFDL CM2.1 and CCSM3 are $4.85\ (\pm\ 0.43) \times 10^{14}\,m^3$ and $4.39\ (\pm\ 0.74) \times 10^{14}\,m^3$, respectively. Both values are close to the mean observed volume but these models have lower variability; in particular, the EDW volume variability in GFDL CM2.1 is about one-third of the value from observations. As opposed to the poor simulation of EDW volume variability, the variability in EDW formation is better reproduced in all three models. The time-mean EDW formation rate and variability from CCSM3 [$6.14\ (\pm\ 2.54)$ Sv $= 1.94\ (\pm\ 0.80) \times 10^{14}\,m^3\,yr^{-1}$] and GFDL CDA [$5.33\ (\pm\ 2.04)$ Sv $= 1.68\ (\pm\ 0.64) \times 10^{14}\,m^3\,yr^{-1}$]

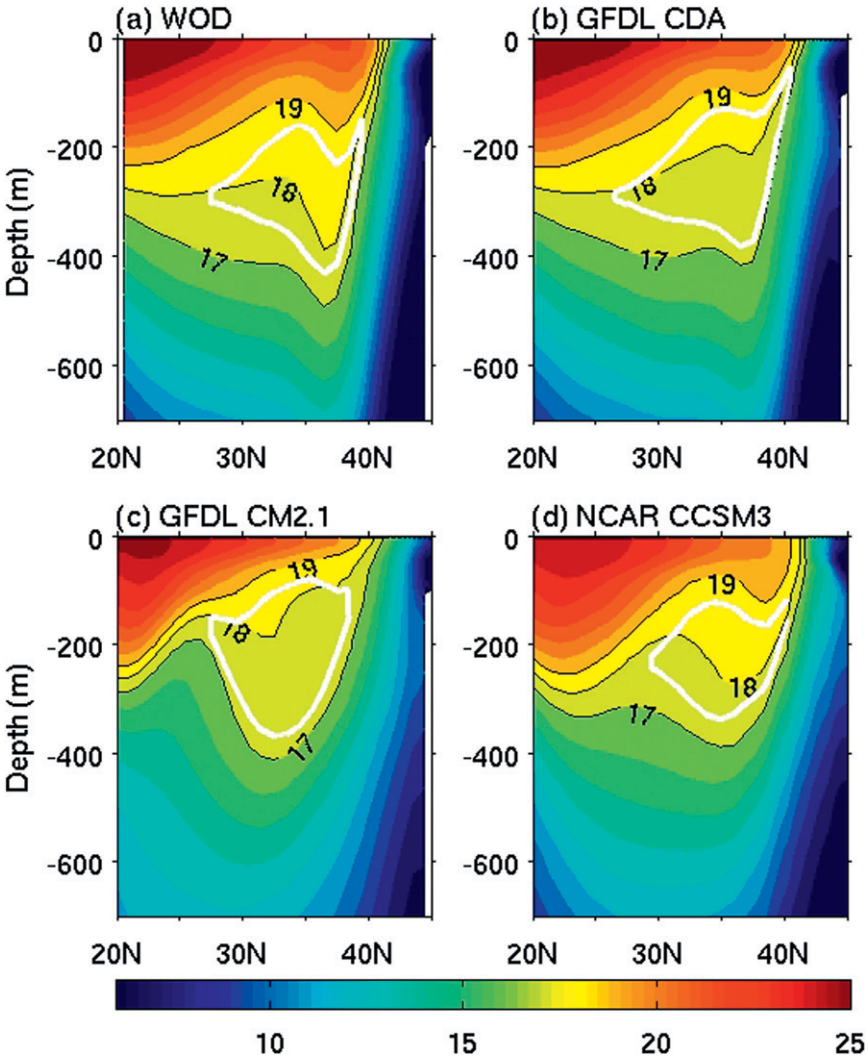

FIG. 2. Temporal-mean temperature sections (°C) along 55°W from (a) WOD, (b) GFDL CDA, (c) GFDL CM2.1, and (d) CCSM3. Black contours are for 17°, 18°, and 19°C isotherms, and white contours indicate the region with a temperature gradient less than 0.006°C m^{-1}.

are close to those estimated from OAFlux data [6.13 (± 2.93) Sv = 1.93 (± 0.92) × 10^{14} m^3 yr^{-1}]. The mean formation rate from GFDL CM2.1 [2.03 (± 2.27) Sv = 0.64 (± 0.72) × 10^{14} m^3 yr^{-1}] is very low compared to the estimate from observations but the variability is comparable with that from observations.

An analysis of the thickness of the EDW from WOD (Fig. 4a) averaged over the study period shows that the thick EDW layer lies along the GS path and within 5° latitude to the south of the GS. The spatial pattern of thickest EDW from GFDL CDA (Fig. 4b) also lies along the GS within the same distance from the GS path. However, the thick layers of EDW from GFDL CM2.1 (Fig. 4c) and CCSM3 (Fig. 4d) are located farther south, particularly for GFDL CM2.1 where the center of the thick EDW is outside this 5°-latitude band. The thickest EDW from both observations and models are located between 60° and 50°W. However, the maximum EDW thicknesses from all three models are larger than that from WOD. On average, the EDW from observations is spread over a larger area than the EDW in GFDL CM2.1 and CCSM3, which explains why the mean volumes from models are comparable with that from observations but the models have thicker EDW layers. Another interesting feature shown in Fig. 4 is that no EDW was found in GFDL CM2.1 to the west of 70°W and in CCSM3 to the west of 65°W just to the south of the GS. This is due to the warm biases (Fig. 5) of SST in the models in those regions, which suppress formation of the EDW.

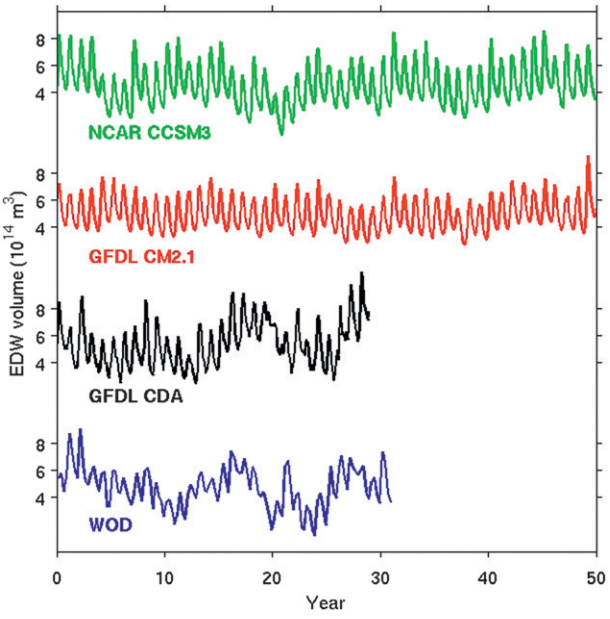

FIG. 3. Time series of the EDW volume (10^{14} m^3) estimated from observations (WOD: blue) and models (GFDL CDA: black; GFDL CM2.1: red; and CCSM3: green).

Estimates from OAFlux SST and air–sea heat fluxes suggest that the formation of EDW is confined to the west of 40°W (Fig. 5a). Consistent with the distribution of the EDW, formation of EDW occurs along the GS with large values just to the south of the GS. The maximum formation is located at 60°W, slightly to the northwest of the thickest EDW. Compared to the area of EDW, the positive formation is constrained in a smaller region to the north of 32°N. Although all three models give thick EDW, the maximum formation rates from the models (Fig. 5) are lower than that estimated from observations. Similar to the EDW thickness, GFDL CDA gives the best simulation of the formation rate in terms of spatial structure (Fig. 5b), though the region with large formation is farther to the south compared to the observations. The EDW formation region in GFDL CM2.1 and CCSM3 is spatially limited to the west of 50°W unlike in the observations, with large formation values to the west of 60°W. Consistent with the distribution of EDW volume, there is no EDW formed in GFDL CM2.1 to the west of 70°W and CCSM3 west of 65°W just to the south of the GS as a result of warm biases of SST in the models. Two conditions are essential for EDW formation: heat loss to the atmosphere and outcrop of the 19°C isotherm. Although the heat loss condition is satisfied in the models, no EDW can be formed without outcropping of the 19°C isotherm, which explains why the warm biases prevent the formation of EDW in the western region close to the GS.

The formation of EDW is closely linked to the air–sea heat fluxes. Unlike the observed eastward extension of the strong heat loss to the atmosphere along the GS (Fig. 6a), the strong heat release from the ocean is constrained to the west in the two models without data assimilation (Figs. 6c,d). In particular, the large heat loss in GFDL CM2.1 is confined mostly to the west of 60°W. In addition, the net air–sea heat flux in GFDL CM2.1 is much weaker than the net flux from OAFlux (Fig. 6a). These differences in the air–sea heat fluxes explain the weak and more spatially constrained EDW formation in the models. The heat flux from CCSM3 in the region close to the GS is comparable with OAFlux. However, the outcropping of the 19°C isotherm is confined to the west of 60°W, which explains the lack of formation of EDW to the east in CCSM3. This suggests that the outcropping region south of the GS plays an important role in the formation of EDW in CCSM3.

The differences in spatial distribution of EDW and its formation between data and models also can be caused by the velocity fields. The surface velocity from the altimeter shows that the strong eastward flow associated with the GS is concentrated in a very narrow band and strong flow can be seen to the east of 50°W (Fig. 7a). The strong GS carries warm water to the east, so that the 19°C isotherm outcrop extends to 50°W and farther to the east during early formation season despite seasonal cooling. However, in all three models the GS flow is weak compared to altimeter measurements and the relatively strong flow is confined to the west of 65°W (Figs. 7b–d). The weak GS is unable to transport warm water to the east efficiently enough to precondition the eastern region for mode water, which explains why the formation rate is weak and confined to the west in the models. Another important difference between GS in

TABLE 1. EDW volume statistics from observations (WOD) and models (GFDL CDA, GFDL CM2.1, and CCSM3). Mean (and std dev) volume of nonseasonal anomalies. Also shown is the time-mean (and std dev) EDW formation rate. Note that 1 Sv ≡ 10^6 m^3 s^{-1}.

	WOD or OAFlux	GFDL CDA	GFDL CM2.1	CCSM3
Mean EDW volume (10^{14} m^3)	4.71 (± 1.12)	5.25 (± 1.09)	4.85 (± 0.43)	4.39 (± 0.74)
EDW variability due to thickness (Sv)	0.60	0.74	0.31	0.49
EDW variability due to area (Sv)	0.67	0.57	0.31	0.41
EDW formation rate (Sv)	6.13 (± 2.93)	5.33 (± 2.04)	2.03 (± 2.27)	6.14 (± 2.54)

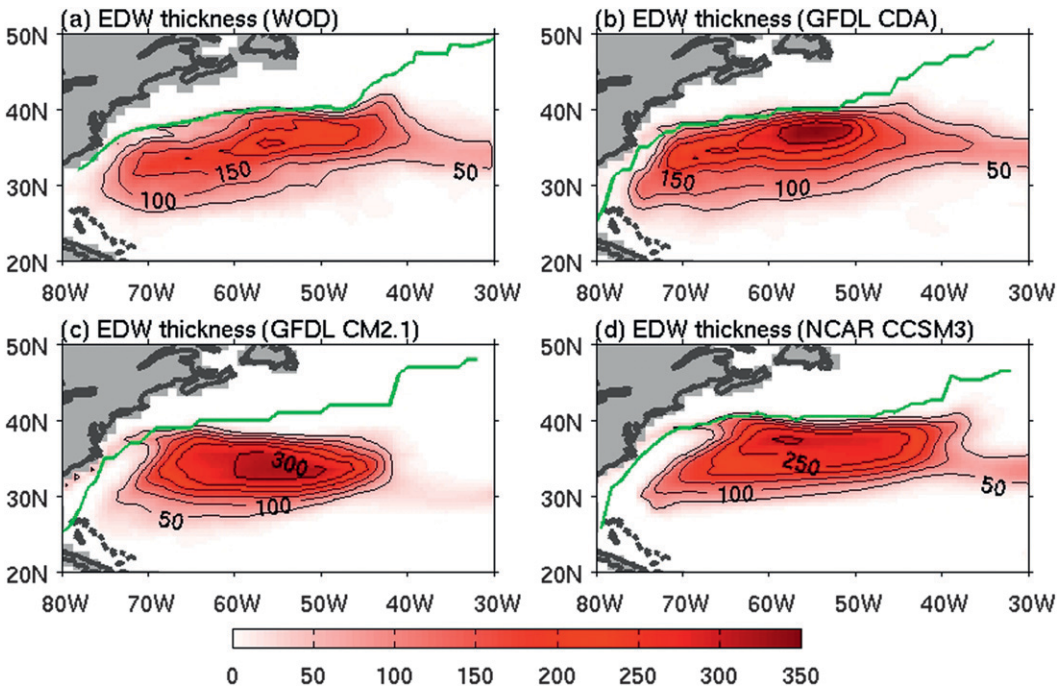

FIG. 4. Spatial distribution of the temporal mean thickness (m) of EDW for (a) WOD, (b) GFDL CDA, (c) GFDL CM2.1, and (d) CCSM3. Green lines indicate the corresponding mean GS path.

the observations and models is that in all three models the GS jet is excessively wide with eastward flow in a 10°-latitude band versus the less-than-2°-latitude band in observations. This excessively wide GS in the models effectively spreads the EDW into the subtropical region, explaining the thick EDW layer in the eastern region where less EDW is formed. Equally important is that the recirculation gyre just to the south of the GS to the north of 35°N is missing in all three models, which also contributes to the wide spread of the EDW from its formation region in the models.

b. Seasonal cycle

Monthly Argo temperature data are used to better resolve the seasonal evolution of the EDW volume, for comparison with results from models. On seasonal time scales, the EDW volume estimated from Argo temperature data (Fig. 8) shows a maximum in April with a sharp increase during January and February and a slow decrease from April to October. The maximum EDW volume in all three models occurs in March. A large part of the seasonal variation in the EDW volume can be explained by changes in EDW layer thickness, about 90% for observations and GFDL CDA and 80% for GFDL CM2.1 and CCSM3 (not shown), whereas the EDW area change only accounts for a small portion of the seasonal EDW volume change. As found in Kwon (2003), this suggests that vertical erosion plays a dominant role in the seasonal destruction of EDW.

Consistent with the seasonal variations in EDW volume, the formation rate from OAFlux is positive before April with the maximum formation rate during February (Fig. 9). The seasonal cycle of the formation rate from GFDL CDA is in phase with that from OAFlux, though the maximum formation during February is smaller. Similar to the phase shift of EDW volume in CCSM3 and GFDL CM2.1, the maximum formation rate also occurs earlier in the two models than that derived from OAFlux. This phase difference in EDW formation is not explained by the net air–sea heat flux, because the seasonal evolution of air–sea heat fluxes from all three models is in phase with the heat flux from OAFlux, with the maximum heat loss in December. The phase differences in EDW formation can be attributed to the cold biases east of 70°W in GFDL CM2.1 and CCSM3, which provide relatively large outcropping areas for EDW formation during early winter compared to the observations and GFDL CDA. The cold bias in the east in the models may, in turn, be related to the weak and less energetic GS system, which is unable to efficiently carry warm water to the east and mix with surrounding water.

It is difficult to examine the budget of EDW volume with available data and model outputs, in particular because of the difficulty in determining the destruction

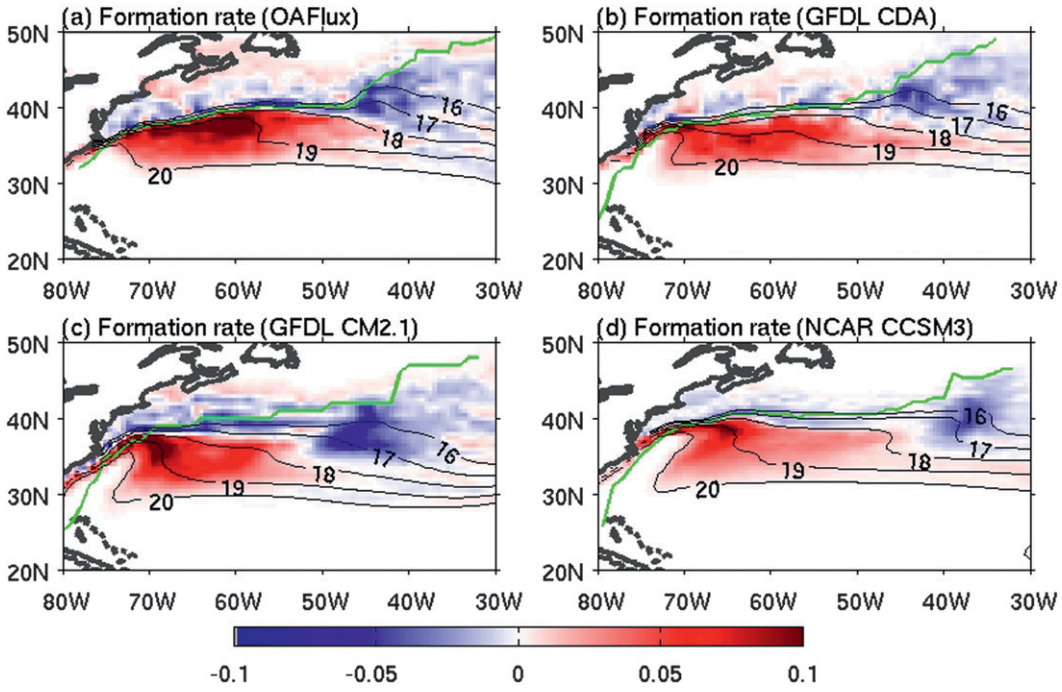

FIG. 5. Temporal-mean formation rate of the EDW (Sv) from (a) OAFlux, (b) GFDL CDA, (c) GFDL CM2.1, and (d) CCSM3. Positive (negative) values are shown in red (blue) and indicate net volume gain (loss) in the 17°–19°C class. Green lines indicate the corresponding mean GS path and black lines are the mean 16°–19°C isotherm contours.

of EDW through mixing. However, Figs. 8 and 9 indicate that the EDW increase during the formation season from GFDL CM2.1 follows the cumulative EDW formation well, suggesting that the oceanic processes (advection and mixing) play a minimal role in EDW volume change during the formation season on average in our study region. This is confirmed by the weak transport of 17°–19°C waters across the boundaries in GFDL CM2.1. The total formation of EDW during the formation season from observations as well as from GFDL CDA and CCSM3 is considerably larger than the corresponding EDW volume increase. The transport of 17°–19°C waters across the boundaries in CCSM3 is also very weak, which implies that part of the EDW formed during the formation season is destroyed through mixing at the same time. Another factor contributing to the difference between EDW volume and formation is the vertical stratification constraint, where part of the newly formed 17°–19°C water may not meet the stratification criterion and therefore contributes to the difference. While in GFDL CDA the transport of 17°–19°C waters out of the study region explains one-third of the difference between total formation and EDW volume increase during the formation season, implying that the mixing also plays an important in EDW destruction. We are unable to compute the transport term from observations because of the lack of subsurface velocity fields. However, it is likely that the mixing plays an important role in the EDW destruction based on the results from a simply model presented in Kelly and Dong (2013), although the focus of that study is for interannual variations.

c. *Temporal variability*

In section 3a, we showed that the variability of EDW volume from the two models without data assimilation (GFDL CM2.1 and CCSM3) is quite low compared to the observed values, though the variability in the formation rate is well captured in all three models. The lack of variability in EDW volume from models is therefore related to the oceanic processes in the models. Qiu et al. (2007) suggested that the mesoscale eddies play an important role in the destruction of STMW through mixing in the Kuroshio Extension region. It is well known that the GS region is among the regions with the strongest eddy activity in the world oceans as observed from satellite altimetry measurements (Fig. 10). This strong eddy activity in the GS region is poorly represented in all three models, which do not show the high eddy kinetic energy (EKE) near the GS (Fig. 10). The inability of the models to capture the strong eddy activity and its year-to-year variability could explain the weak variability of EDW volume. The weak circulation in the models may also affect the variability through advection, which

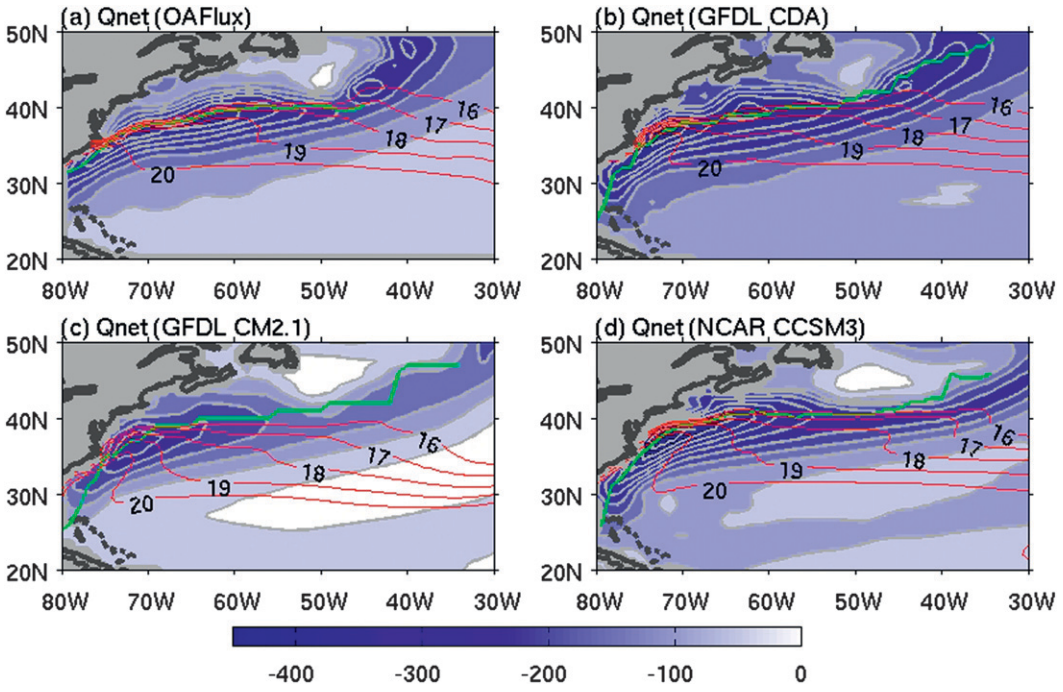

FIG. 6. Wintertime (JFM) air–sea heat fluxes ($W\,m^{-2}$) from (a) OAFlux, (b) GFDL CDA, (c) GFDL CM2.1, and (d) CCSM3. Green lines indicate the corresponding mean GS path and red lines indicate 17°–19°C isotherms.

contributes to outcrop variability and through subduction of EDW away from the GS region. The variability of EDW volume in the data-assimilation GFDL CDA is close to the value estimated from WOD despite the lack of eddy activity. This could be simply because of the assimilation of temperature profiles, which corrects the readily observed variable, that is, EDW volume, but is not be able to simulate the dynamic processes.

As in the seasonal variations of EDW volume, both the area and layer thickness can cause changes on interannual time scales. To further examine whether the weak variability in the models is due to lack of change in the area or in the layer thickness, we compute the contributions of area and thickness to the EDW volume variability. The thickness contribution to EDW volume variability is computed based on the product of time-varying thickness H and time-mean area $\overline{A}$, whereas the contribution from area is computed as $\overline{HA}$. Unlike for the seasonal cycle of EDW volume in which layer thickness dominates, both EDW area and thickness are important to the variability of the EDW volume from WOD, with contributions from the area being slightly larger than those from the thickness (Table 1). Both the area and thickness also contribute significantly to the variability of EDW volume in GFDL CDA, but unlike in the observations, the thickness has a larger influence. In GFDL CM2.1, variations in the area and thickness contribute equally to the variability of EDW volume, but the variability from both is considerably lower than that from the observations, suggesting that the lower variability in EDW volume in the model is related to both area and thickness with relatively more contribution from area. Variability of EDW volume as a result of area and thickness changes in CCSM3 is also lower than the observed values with changes in thickness contributing more to the model bias in EDW volume variability. Both air–sea heat flux and oceanic processes (advection and mixing) contribute to changes in the EDW thickness and area. However, we expect that the EDW thickness would be largely controlled by the vertical convection owing to heat loss to the atmosphere, whereas the oceanic processes would have a strong influence on the EDW area through propagation/subduction and eddy mixing. The larger contribution from area to the biases in EDW volume variability suggests that the oceanic processes are not well represented in the models. This is consistent with the weak eddy activity in the models.

Although the formation variability cannot explain the weak variability of EDW volume in GFDL CM2.1 and CCSM3, this does not eliminate the actual influence of changes in formation on EDW volume. To examine this relationship we computed the EDW volume change ΔV from one year to the next during the formation season and the total formation during the same period. The yearly difference of EDW volume is taken between spring (AMJ) and the previous summer (JAS) to capture the

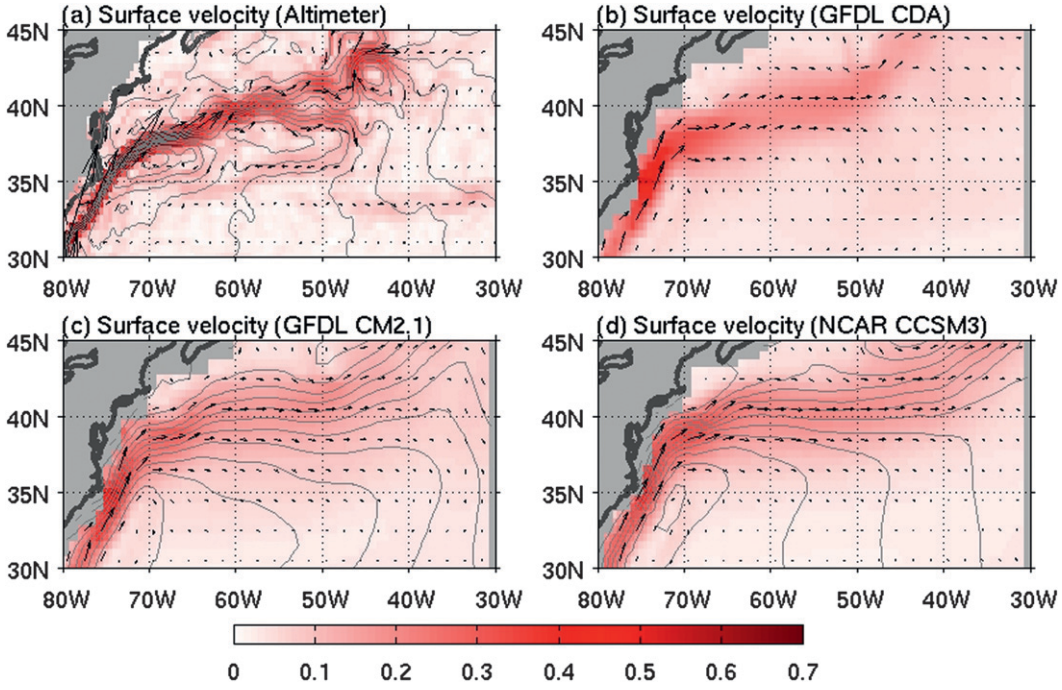

FIG. 7. Temporal-mean surface velocity fields ($m\,s^{-1}$) from (a) altimeter, (b) GFDL CDA, (c) GFDL CM2.1, and (d) CCSM3. Color maps indicate the speed of the current and the arrows indicate the direction of the current. Gray lines are mean SSH contours with interval of 0.1 m.

full formation season. The total formation is integrated from JAS to JFM. Our results show that the observed changes in the EDW volume are significantly correlated with the EDW formation, with a correlation of 0.55 exceeding the 95% significance level of 0.35. The data-assimilation model captures the relationship between EDW volume change and formation well, experiencing a correlation of 0.65 (0.36). The correlations from GFDL CM2.1 and CCSM3 are 0.39 and 0.78, respectively, both above the 95% significance level of 0.28. We also reached the same conclusion using the monthly data from models but with slightly higher correlations for all three models, where the formation is integrated from August to March to cover the entire formation period and the EDW volume change is taken as the difference between April and previous August.

What is interesting is the difference between model and data in the spatial structure of the variability of EDW layer thickness. Here, the standard deviation of the EDW layer thickness at each grid point is computed to illustrate the variability of EDW thickness. The largest variability in EDW thickness from WOD (Fig. 11a) is located between 50° and 60°W, collocated with the region where the thickest EDW is found. Although the time-mean EDW layer is thicker in all three models compared to estimates from WOD (Fig. 3), the variability of EDW thickness in models is weaker. The spatial structure of EDW variability in GFDL CDA is somewhat similar to that from observations, except that the variability is stronger to the west of 60°W (Fig. 11b). The variability of EDW thickness from GFDL CM2.1 shows a very different spatial pattern from the observed distribution (Fig. 11c), with strong variability to the eastern and western sides of the region where the EDW is the thickest. In contrast with the observations, the variability of EDW

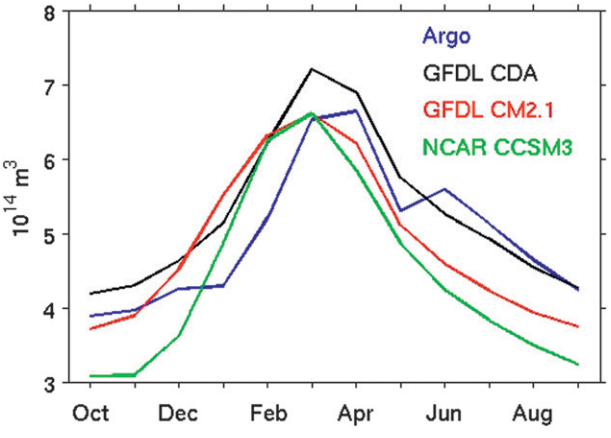

FIG. 8. Seasonal variations of the EDW volume estimated from Argo temperature measurements (blue), coupled data-assimilation GFDL CDA (black), GFDL CM2.1 (red), and CCSM3 (green).

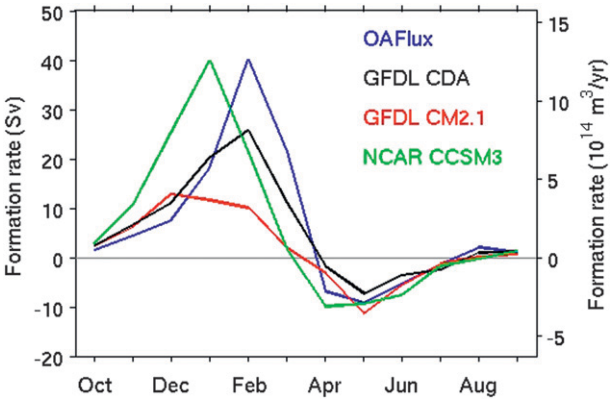

FIG. 9. Seasonal variations of the EDW formation rate from OAFlux (blue), coupled data-assimilation GFDL CDA (black), GFDL CM2.1 (red), and CCSM3 (green).

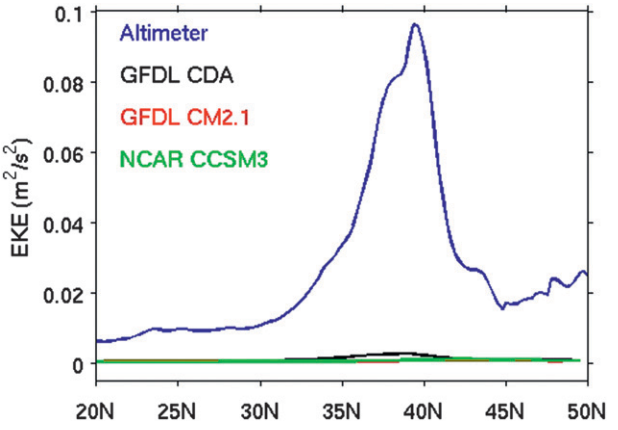

FIG. 10. Zonally (30°–80°W) averaged EKE [$=(u'^2 + v'^2)/2$] derived from satellite altimeter measurements (blue), coupled data-assimilation GFDL CDA (black), GFDL CM2.1 (red), and CCSM3 (green).

thickness is weak in the region of the thickest EDW. Although the strongest EDW variability in CCSM3 coincides with the region where the EDW layer is thick, the strong EDW variability is confined to the northern part of the thick EDW region.

Both dynamic and thermodynamic processes can induce differences in the spatial distribution of variability of EDW thickness, including formation, mixing, and oceanic advection. The formation of EDW shows large variability around the GS path in both the observations and models (not shown), but formation cannot explain the spatial structure of the variability of EDW thickness in the models. This suggests that the oceanic processes (mixing and advection) are responsible for EDW thickness variability in the models. As we discussed earlier, the observed strong eddy activity in the GS region is poorly represented in the models. This lack of eddy activity in the models results in weak mixing, which may contribute to the weak variability in the EDW thickness. The ocean

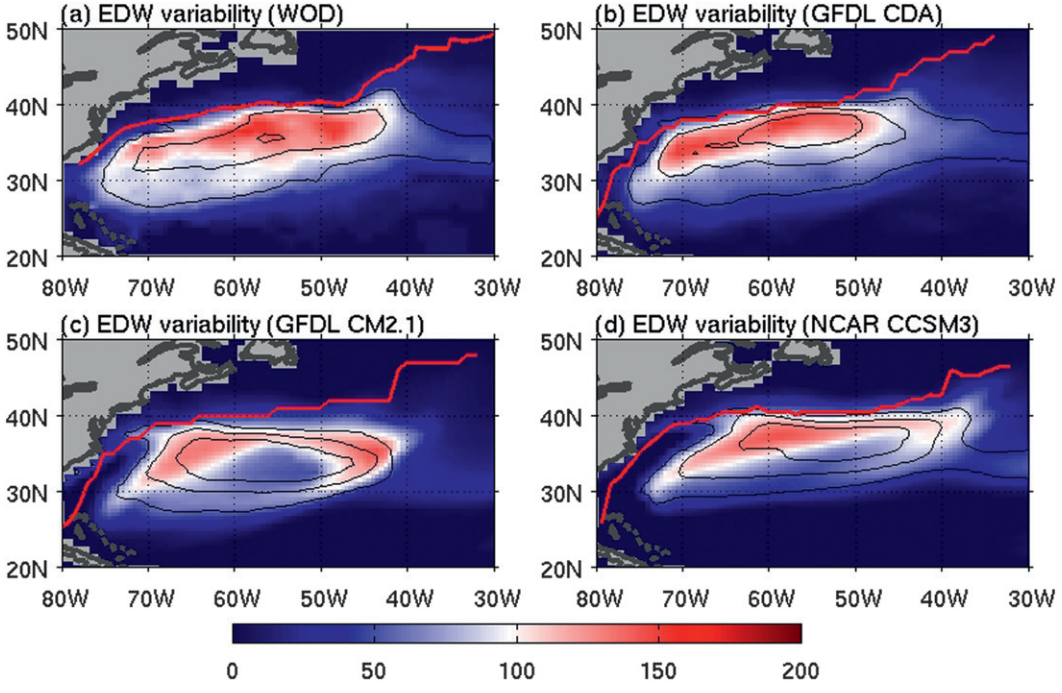

FIG. 11. Std dev of EDW thickness (m) estimated from (a) WOD, (b) GFDL CDA, (c) GFDL CM2.1, and (d) CCSM3. Black contours are the corresponding mean thickness of EDW. Red lines denote the mean GS path.

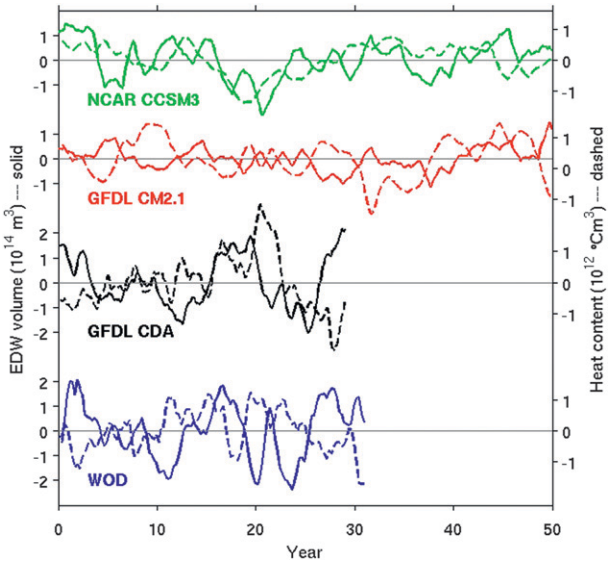

FIG. 12. Time series of anomalous EDW volume (solid lines) and 700-m upper-ocean heat content (dashed lines) from observation (WOD) and models (GFDL CDA, GFDL CM2.1, and CCSM3). Data have been smoothed to remove signals with periods less than a year. Both EDW volume and heat content are computed for the region 25°–45°N, 30°–80°W.

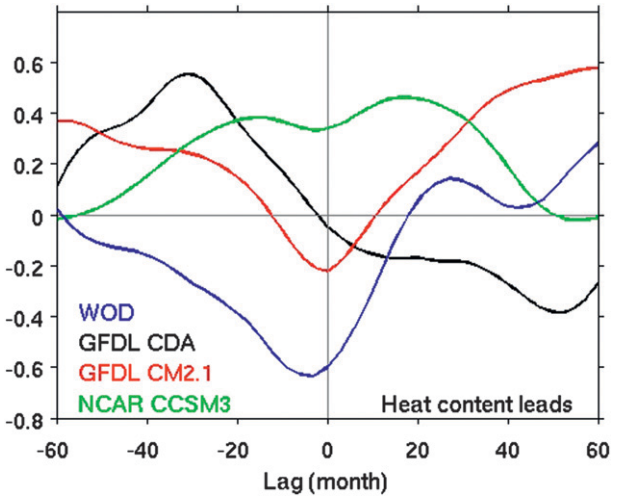

FIG. 13. Lagged correlation between 700-m upper-ocean heat content and the volume of the EDW from observations (WOD: blue) and models (GFDL CDA: black; GFDL CM2.1: red; and CCSM3: green).

circulation may also play a role in the distribution of variability of EDW thickness in the two models without data assimilation. For example, the thick EDW in GFDL CM2.1 (Fig. 3c) is located in the center of the subtropical gyre (Fig. 7c) where the velocity is close to zero, which implies weak influence of the ocean advection on EDW variability in the region. In contrast, the relatively strong variability of EDW thickness surrounding the region of thick EDW follows closely the subtropical gyre circulation in the model, suggesting the importance of oceanic advection in EDW variability in the model.

4. Discussion

How well models reproduce the EDW properties is important as changes in EDW reflect various dynamic and thermodynamic processes. More importantly, as a deficit heat reservoir (low heat content corresponds to large EDW volume), changes in the EDW can modulate both surface and subsurface temperatures regionally and in remote regions. Changes in the EDW can also impose a thermal forcing on the overlying atmosphere. Thus, it is also important to correctly simulate the relationship between upper-ocean heat content and EDW. Figure 12 shows the interannual variations of the EDW volume and the heat content in the upper 700 m from the WOD and all three models. The lagged correlation between the heat content and the volume of EDW from observations and models is shown in Fig. 13. Consistent with previous studies (Kwon 2003; Dong et al. 2007; Douglass et al. 2013) there is an anticorrelation of −0.63 (0.25) between the two variables from WOD, with the EDW volume leading the upper-ocean heat content by 2–3 months. Only GFDL CM2.1 captures the same relationship between the two variables with a statistically significant but lower correlation of −0.22 (0.20). Although the numerical model for GFDL CDA is the same as for GFDL CM2.1, the data-assimilation process alters the observed relationship between the upper-ocean heat content and EDW volume, so that no statistically significant correlation is found between the two variables in GFDL CDA. In contrast with the observed anticorrelation, the upper-ocean heat content from CCSM3 shows a significant positive correlation (0.35) with the EDW volume at zero lag.

To understand the different relationship between the volume of EDW and the upper-ocean heat content from observations and models, we computed the center depth of the EDW layer and examined its relationship with the EDW volume. The volume of EDW from WOD is anticorrelated with the depth of EDW, that is, a shallower EDW layer corresponding to a positive EDW volume anomaly. This suggests that the EDW thickness increases by removing warmer water at the top of the layer, explaining the anticorrelation between the volume of EDW and heat content. These results from WOD are consistent with our previous finding (Dong et al. 2007) that a deep and thin 18°C layer corresponds to a positive heat content anomaly. Interestingly for all three models, the EDW volume is positively correlated

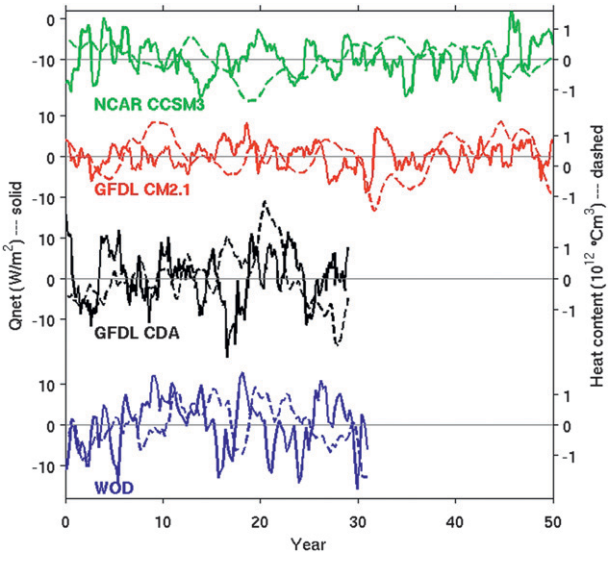

FIG. 14. Time series of anomalous surface heat flux (solid lines) and 700-m upper-ocean heat content (dashed lines) from observation (WOD: blue) and models (GFDL CDA: black; GFDL CM2.1: red; and CCSM3: green). Data have been smoothed to remove signals with periods less than a year.

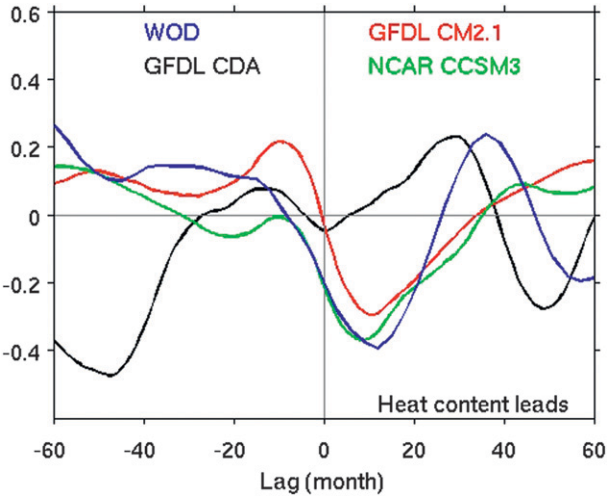

FIG. 15. Lagged correlation between the 700-m upper-ocean heat content and air–sea heat flux from observations (WOD: blue) and models (GFDL CDA: black; GFDL CM2.1: red; and CCSM3: green).

with the depth of EDW; that is, the EDW thickness increases by removing colder water below, thereby increasing the upper-ocean heat content. This explains the predominantly positive correlations between the EDW volume and heat content in the models.

How much heat can be fluxed to the atmosphere from the ocean depends on how much heat is stored in the upper ocean. Indeed, an examination of observations suggests a robust anticorrelation of −0.39 (0.25) between upper-ocean heat content and air–sea heat flux (Fig. 14), with positive heat content anomalies leading heat loss to the atmosphere by about a year (Fig. 15). This anticorrelation is well represented by GFDL CM2.1 and CCSM3, with peak correlations of −0.30 (0.20) and −0.37 (0.20), respectively, when the upper-ocean heat content leads the air–sea heat flux by 10 months. However, the upper-ocean heat content from GFDL CDA does not show a significant anticorrelation with the air–sea heat flux, suggesting that the observed thermal response of overlying atmosphere to the ocean is not captured by the model. The misrepresentation of the thermal response in GFDL CDA is likely related to the cold biases in the model, resulting in heat being added into the ocean during the data-assimilation process. This added heat, particularly during winter, would increase heat content, changing the relationship between variables. Again, this indicates that the data-assimilation process degrades the model's thermodynamic response to forcing. Therefore, caution should be used when using data-assimilation products for diagnostic studies.

The differences between models and observations are also seen in the persistence of SST, heat content, and mode water anomalies. The persistence is examined using the decorrelation time scale, which is defined here as the time over which neighboring data points (in time) are correlated at 95% significance level, which is about 0.3 for our case. Although the volumes of EDW from both models and observations show similar decorrelation time scales, the models show relatively longer decorrelation time scales for SST and upper-ocean heat content compared to those from observations. Although GFDL CDA properly captures the decorrelation scale in the SST, the data-assimilation process did not shorten the time scales of the upper-ocean heat content. The observed upper-ocean heat content shows a decorrelation time scale of two years, whereas the decorrelation time scales from models are greater than three years, particularly the decorrelation time scale in CCSM3, which exceeds four years. Interestingly, the air–sea heat fluxes from OAFlux show a decorrelation time scale about one and half years, whereas the model surface heat fluxes have a decorrelation time scale about a year. These time-scale discrepancies suggest that the intense atmosphere–ocean coupling near the GS is not well represented in the models.

5. Conclusions

The EDW properties from three coupled climate models are compared with those from observations to

evaluate the models' representation of oceanic physics. Our analyses indicate that the models give similar mean EDW volumes compared with the WOD. However, the variability of EDW volume from the two models without data assimilation (GFDL CM2.1 and CCSM3) is too weak. In particular, the EDW variability in GFDL CM2.1 is less than 40% of the observed values, whereas CCSM3 captures about 65% of the observed variability. Both EDW layer thickness and area contribute to the weak EDW variability in the models. The variability of formation rates from all three models are comparable to that estimated from OAFlux. Thus, the weak EDW variability in the models is due to oceanic processes, likely related to the weak eddy activity and weak circulation in the GS region in the models. The mean formation rates from GFDL CDA and CCSM3 are close to the value estimated from OAFlux. However, the mean formation rate from GFDL CM2.1 is very low, less than one-third of the formation rate from OAFlux, although its variability is comparable to that from OAFlux. This weak formation in GFDL CM2.1 is primarily due to the weak air–sea heat flux in the model.

The data-assimilating GFDL CDA gives a better representation of the spatial distribution of EDW and its thickness, with thick EDW within 5° latitude of the GS, whereas the regions of thick EDW from GFDL CM2.1 and CCSM3 are more widely distributed instead of following the GS. The spatial distribution of EDW variability is also well simulated in GFDL CDA, with the largest variability along the GS path, collocated with the thick EDW. This collocation of thick EDW and large variability is not captured by GFDL CM2.1; instead the region of thick EDW has the lowest variability. The collocation is better represented in CCSM3, although the strong EDW variability is confined to the northern part of the thick EDW region. The GFDL CDA also gives a better representation of the spatial distribution of the EDW formation, although the maximum formation rate observed just to the south of the GS is not well captured. The formation rate from the non-data-assimilation models is spatially limited to the west of 50°W. Both the distribution of the air–sea heat fluxes and the outcrop of the 19°C isotherm contribute to the limited formation region for GFDL CM2.1. The air–sea heat fluxes from CCSM3 near the GS are similar to the fluxes from OAFlux, but the formation is affected by the limited 19°C outcrop region because of the lack of warm water transport by the weak GS. Unlike the observed dominant southward movement of the EDW, the EDW in GFDL CM2.1 and CCSM3 moves eastward after formation in the excessively wide Gulf Stream in the models. Those problems with the oceanic processes are typical of coarse-resolution models. High-resolution eddy-resolving models are required to better reproduce physical processes in the strong boundary current regions.

Despite the better representation of the EDW and of formation, the data-assimilating model does not capture the observed thermal response of air–sea heat flux to the upper-ocean heat content. The robust anticorrelation between the upper-ocean heat content and air–sea heat flux is well captured by GFDL CM2.1 and CCSM3, but not by GFDL CDA. The GFDL CM2.1 also captures the observed anticorrelation between the upper-ocean heat content and the EDW volume, which, again, is not captured by GFDL CDA. This suggests that data assimilation degrades the model's thermodynamic response to forcing. We note that the configuration of the ocean component in GFDL CM2.1 and GFDL CDA is the same. Although data assimilation corrects the variables that are readily observed, it changes the relationship between forcing and response. The models experience shorter decorrelation time scales in air–sea heat flux and longer decorrelation time scales in upper-ocean heat content compared with values estimated from observations, suggesting that the intense atmosphere–ocean coupling near the GS is not well represented in the models. Therefore, caution should be used when using data-assimilation products for diagnostic studies.

Acknowledgments. The authors thank the two anomalous reviewers for their insightful comments and suggestions. This work has benefited from many conversations with other CLIMODE investigators. KAK was supported by the National Science Foundation through Grant 0960648 (CLIMODE analysis). SD was supported by the National Science Foundation through Grant 0958548 (CLIMODE analysis), and Atlantic Oceanographic and Metrological Laboratory, NOAA.

REFERENCES

Alexander, M. A., and C. Deser, 1995: A mechanism for the recurrence of wintertime midlatitude SST anomalies. *J. Phys. Oceanogr.,* **25,** 122–137.

Bigorre, S. P., R. A. Weller, J. B. Edson, and J. D. Ware, 2013: A surface mooring for air–sea interaction research in the Gulf Stream. Part II: Analysis of the observations and their accuracies. *J. Atmos. Oceanic. Technol.,* **30,** 450–469.

Danabasoglu, G., W. G. Large, J. J. Tribbia, P. R. Gent, B. P. Briegleb, and J. C. McWilliams, 2006: Diurnal coupling in the tropical oceans of CCSM3. *J. Climate,* **19,** 2347–2365.

Davis, X. J., F. Straneo, Y.-O. Kwon, K. A. Kelly, and J. M. Toole, 2013: Evolution and formation of North Atlantic Eighteen Degree Water in the Sargasso Sea from moored data. *Deep-Sea Res.,* **91,** 11–24.

de Coëtlogon, G., and C. Frankignoul, 2003: On the persistence of winter sea surface temperature in the North Atlantic. *J. Climate,* **16,** 1364–1377.

Delworth, T. L., and Coauthors, 2006: GFDL CM2 global coupled climate models. Part I: Formulation and simulation characteristics. *J. Climate,* **19,** 643–674.

Dong, S., and K. A. Kelly, 2004: Heat budget in the Gulf Stream region: The importance of heat storage and advection. *J. Phys. Oceanogr.,* **34,** 1214–1231.

——, S. Hautala, and K. A. Kelly, 2007: Interannual variations in upper-ocean heat content and heat transport convergence in the western North Atlantic. *J. Phys. Oceanogr.,* **37,** 2682–2697.

Douglass, E. M., Y.-O. Kwon, and S. R. Jayne, 2013: A comparison of subtropical mode waters in a climatologically-forced model. *Deep-Sea Res.,* **91,** 139–151.

Ducet, N., P.-Y. Le Traon, and G. Reverdin, 2000: Global high-resolution mapping of ocean circulation from TOPEX/Poseidon and *ERS-1* and *-2. J. Geophys. Res.,* **105,** 19 477–19 498.

Forget, G., G. Maze, M. Buckley, and J. Marshall, 2011: Estimated seasonal cycle of North Atlantic Eighteen Degree Water volume. *J. Phys. Oceanogr.,* **41,** 269–286.

Hanawa, K., and L. Talley, 2001: Mode waters. *Ocean Circulation and Climate,* J. Siedler, J. Church, and J. Gould, Eds., International Geophysics Series, Vol. 77, Academic Press, 373–386.

Joyce, T., C. Deser, and M. A. Spall, 2000: The relation between decadal variability of subtropical mode water and the North Atlantic Oscillation. *J. Climate,* **13,** 2550–2569.

——, L. N. Thomas, W. K. Dewar, and J. B. Girton, 2013: Eighteen Degree Water formation within the Gulf Stream during CLIMODE. *Deep-Sea Res.,* **91,** 1–10.

Kelly, K. A., and S. Dong, 2013: The contributions of atmosphere and ocean to North Atlantic subtropical mode water volume anomalies. *Deep-Sea Res. II,* **91,** 111–127.

——, R. J. Small, R. Samelson, B. Qiu, T. M. Joyce, M. Cronin, and Y.-O. Kwon, 2010: Western boundary currents and frontal air–sea interaction: Gulf Stream and Kuroshio Extension. *J. Climate,* **23,** 5644–5667.

Kwon, Y.-O., 2003: Observation of general circulation and water mass variability in the North Atlantic Subtropical Mode Water region. Ph.D. thesis, University of Washington, Seattle, WA, 161 pp.

——, and S. C. Riser, 2004: North Atlantic subtropical mode water: A history of ocean–atmosphere interaction 1961–2000. *Geophys. Res. Lett.,* **31,** L19307, doi:10.1029/2004GL021116.

Levitus, S., J. I. Antonov, T. P. Boyer, R. A. Locarnini, H. E. Garcia, and A. V. Mishonov, 2009: Global ocean heat content 1955–2008 in light of recently revealed instrumentation problems. *Geophys. Res. Lett.,* **36,** L07608, doi:10.1029/2008GL037155.

Marshall, J., and Coauthors, 2009: Observing the cycle of convection and restratification over the Gulf Stream and the subtropical gyre of the North Atlantic Ocean: Preliminary results from the CLIMODE field campaign. *Bull. Amer. Meteor. Soc.,* **90,** 1337–1350.

Maze, G., and J. Marshall, 2011: Diagnosing the observed seasonal cycle of Atlantic subtropical mode water using potential vorticity and its attendant theorems. *J. Phys. Oceanogr.,* **41,** 1986–1999.

——, G. Forget, M. Buckley, J. Marshall, and I. Cerovecki, 2009: Using transformation and formation maps to study the role of air–sea fluxes in North Atlantic Eighteen Degree Water formation. *J. Phys. Oceanogr.,* **39,** 1818–1835.

——, J. Deshayes, J. Marshall, A. Tréguier, A. Chronis, and L. Vollmer, 2013: Surface vertical PV fluxes and subtropical mode water formation in an eddy-resolving numerical simulation. *Deep-Sea Res.,* **91,** 128–138.

McCartney, M. S., 1982: The subtropical recirculation of mode waters. *J. Mar. Res.,* **40** (Suppl.), 427–464.

Nakamura, M., and S. Yamane, 2009: Dominant anomaly patterns in the near-surface baroclinicity and accompanying anomalies in the atmosphere and oceans. Part I: North Atlantic basin. *J. Climate,* **22,** 880–904.

Olsina, O., N. Wienders, and W. K. Dewar, 2013: An estimate of the climatology and variability of Eighteen Degree Water potential vorticity forcing. *Deep-Sea Res.,* **91,** 84–95.

Qiu, B., S. Chen, and P. Hacker, 2007: Effect of mesoscale eddies on subtropical mode water variability from the Kuroshio Extension System Study (KESS). *J. Phys. Oceanogr.,* **37,** 982–1000.

Rio, M.-H., and F. Hernandez, 2004: A mean dynamic topography computed over the world ocean from altimetry, in situ measurements, and a geoid model. *J. Geophys. Res.,* **109,** C12032, doi:10.1029/2003JC002226.

Roemmich, D., and W. B. Owens, 2000. The Argo Project: Global ocean observations for understanding and prediction of climate variability. *Oceanography,* **13,** 45–50.

——, and J. Gilson, 2009: The 2004–2008 mean and annual cycle of temperature, salinity, and steric height in the global ocean from the Argo Program. *Prog. Oceanogr.,* **82,** 81–100.

Schiffer, R. A., and W. B. Rossow, 1983: The International Satellite Cloud Climatology Project (ISCCP): The first project of the World Climate Research Programme. *Bull. Amer. Meteor. Soc.,* **64,** 779–784.

Suga, T., K. Motoki, Y. Aoki, and A. M. McDonald, 2004: The North Pacific climatology of winter mixed layer and mode waters. *J. Climate,* **34,** 3–22.

Talley, L. D., and M. S. McCartney, 1982: Distribution and circulation of Labrador Sea Water. *J. Phys. Oceanogr.,* **12,** 1189–1205.

——, and M. E. Raymer, 1982: Eighteen Degree Water variability. *J. Mar. Res.,* **40,** 757–775.

Thompson, L., and W. Cheng, 2008: Water masses in the Pacific in CCSM3. *J. Climate,* **21,** 4514–4528.

Timlin, M. S., M. A. Alexander, and C. Deser, 2002: On the reemergence of North Atlantic SST anomalies. *J. Climate,* **15,** 2707–2712.

Walin, G., 1982: On the relation between sea surface heat flow and thermal circulation in the ocean. *Tellus,* **34,** 187–195.

Worthington, L., 1995: The 18° Water in the Sargasso Sea. *Deep-Sea Res.,* **5,** 297–305.

Xie, S.-P., L. Xu, Q. Liu, and F. Kobashi, 2011: Dynamical role of mode water ventilation in decadal variability in the central subtropical gyre of the North Pacific. *J. Climate,* **24,** 1212–1225.

Xu, L., S.-P. Xie, and Q. Liu, 2012a: Mode water ventilation and subtropical countercurrent over the North Pacific in CMIP5 simulations and future projections. *J. Geophys. Res.,* **117,** C12009, doi:10.1029/2012JC008377.

——, ——, ——, and F. Kobashi, 2012b: Response of the North Pacific Subtropical Countercurrent and its variability to global warming. *J. Oceanogr.,* **68,** 127–137.

Yu, L., and R. A. Weller, 2007: Objectively analyzed air–sea heat fluxes for the global ice-free oceans (1981–2005). *Bull. Amer. Meteor. Soc.,* **88,** 527–539.

Zhang, S., M. J. Harrison, A. Rosati, and A. T. Wittenberg, 2007: System design and evaluation of coupled ensemble data assimilation for global oceanic climate studies. *Mon. Wea. Rev.,* **135,** 3541–3564.

——, A. Rosati, and M. J. Harrison, 2009: Detection of multidecadal oceanic variability by ocean data assimilation in the context of a ''perfect'' coupled model. *J. Geophys. Res.,* **114,** C12018, doi:10.1029/2008JC005261.